JOURNAL OF THERMOPHYSICS AND HEAT TRANSFER
Vol. 19, No. 1, January–March 2005

Numerical Simulation of Galileo Probe Entry Flowfield with Radiation and Ablation

Shingo Matsuyama*
Japan Aerospace Exploration Agency, Chofu 182-8522, Japan
and
Naofumi Ohnishi,† Akihiro Sasoh,‡ and Keisuke Sawada§
Tohoku University, Sendai 980-8579, Japan

A trajectory-based heating analysis of the Galileo probe entry flowfield is attempted to reproduce the heat-shield recession data obtained during the entry flight. In the calculation, the mass conservation equations for the freestream gas (hydrogen–helium gas mixture) and the ablation product gas are solved with an assumption of thermochemical equilibrium. The ablation process is assumed to be quasi steady and is coupled with the flowfield calculation. The radiative energy transfer calculation is tightly coupled with the flowfield calculation, where the absorption coefficients of the gas mixture are given by the multiband radiation model having 4781 wavelength points for wavelength range from 750 to 15,000 Å. The injection-induced turbulence model proposed by Park is employed to account for the enhanced turbulence effect due to the ablation product gas. It is shown that the final recession profile of the flight data at the frustum region can be closely reproduced if the injection-induced turbulence model is employed, although that at the stagnation region is overestimated. The cause of the enhanced radiative heating that occurs at the frustum region is given in connection with the enhanced turbulence effect in the shock layer.

Nomenclature

A^+	=	constant in Eq. (12)
C	=	mass concentration
D	=	binary diffusion coefficient, m^2/s
d	=	mixing length, m
$\boldsymbol{F}$	=	x component of convective flux vector
$\boldsymbol{F}_v$	=	x component of viscous flux vector
$\boldsymbol{G}$	=	y component of convective flux vector
$\boldsymbol{G}_v$	=	y component of viscous flux vector
$\boldsymbol{H}$	=	source vector for axisymmetric flow
$\boldsymbol{H}_v$	=	source vector for viscous flow
$\boldsymbol{H}_{\text{rad}}$	=	source vector for radiation
$\dot{m}$	=	mass injection rate, $kg/m^2 \cdot s$
n	=	number density, $1/cm^3$
Q	=	conservative variables
q_c	=	convective heat flux, MW/m^2
q_{rad}	=	radiative heat flux, MW/m^2
Sc	=	Schmidt number
y	=	distance from the wall, m
y^+	=	dimensionless distance from the wall
ΔH_a	=	heat of ablation, MJ/kg
Δs	=	surface recession rate, m/s
κ_λ	=	absorption coefficient at given wavelength, cm^{-1}
σ_λ	=	absorption cross section at given wavelength, cm^2
τ	=	time constant in Eq. (15), 2×10^{-4}s
χ	=	von Kármán constant, 0.4
ω	=	vorticity, s^{-1}

Subscripts

a	=	ablation product gas
BL	=	Baldwin–Lomax turbulence model
f	=	freestream gas
i	=	species i
inj	=	injection-induced turbulence model
sub	=	sublimation
t	=	turbulent
v	=	virgin material
w	=	wall value

Received 20 April 2004; revision received 20 July 2004; accepted for publication 20 July 2004.

*Researcher, Information Technology Center, Institute of Space Technology and Aeronautics; smatsu@chofu.jaxa.jp. Member AIAA.
†Research Associate, Department of Aerospace Engineering.
‡Professor, Ultra-High-Enthalpy Flow Laboratory, Institute of Fluid Science. Associate Fellow AIAA.
§Professor, Department of Aerospace Engineering. Associate Fellow AIAA.

Introduction

THE Galileo probe vehicle entered into the atmosphere of the gaseous giant planet Jupiter at a relative velocity of 47.4 km/s on 7 December 1995. During the deceleration from Mach 50, the peak heating rate and heat load exerted on the forebody heatshield amounted to 300 MW/m^2 and 3000 MJ/m^2, respectively.[1–3] The maximum deceleration was as large as 250 g. No spacecraft has ever experienced such severe entry conditions.

Figure 1 shows the cross section of the Galileo probe vehicle deceleration module.[1–3] The probe configuration is a sphere–cone with 22.2-cm nose radius and 44.86-deg half-angle. There were 10 analog resistance ablation detector (ARAD) sensors embedded in its forebody heatshield, and 4 resistance thermometers were bonded to the inside of the structure.[2,3] Figure 2 shows the locations of ablation sensors (A_1–A_{10}) in the forebody heatshield. The ablator recession data were successfully transmitted via the Galileo orbiter to the Earth after probe entry, and the final recession profile was deduced.[2,3]

Before the entry flight, predictions were made for the entry heating environment.[1] These calculations employed the viscous shock-layer code and assumed thermochemical equilibrium. Radiative heat fluxes were calculated using the spectrally detailed radiation model and also the tangent-slab approximation. The shock-layer flow was assumed to be fully turbulent. In Fig. 3, the comparison of the predicted surface recession and that of the flight data[2,3] are shown. As can be seen, the predicted recession overestimates 30% at the stagnation region, whereas it substantially underestimates over the frustum region.

In the preflight prediction,[1] a two-layer, eddy-viscosity turbulence model based on the mixing-length concept and the

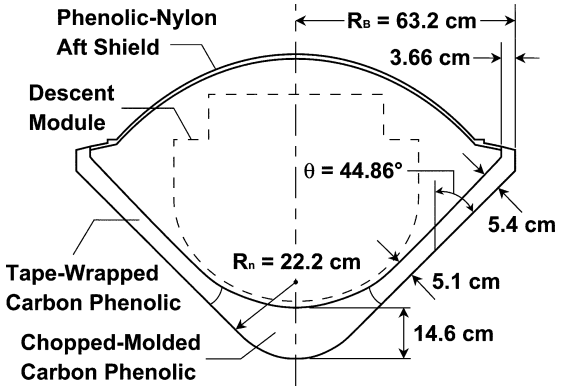

Fig. 1 Cross section of the Galileo Probe vehicle deceleration module.[1–3]

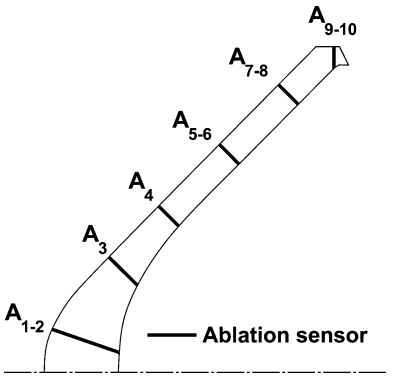

Fig. 2 Locations of 10 ablation sensors.[2,3]

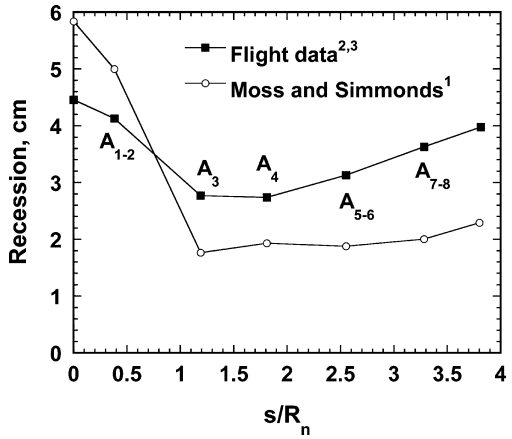

Fig. 3 Comparison of predicted final forebody heatshield recession profile with flight data.

Clauser–Klebanoff expression was employed as the baseline turbulence model. In addition, two different turbulence models were also examined for comparison. One can find, however, that all of these turbulence models actually failed to reproduce the anomalously higher heating rate that appeared at the frustum region. These turbulence models are originally derived for a smooth wall without surface injection. Promotion of turbulence in the boundary layer due to injection of the ablation product gas was pointed out as one clue to reproduce the flight data at the frustum region.[4]

In Ref. 5, Park assumed that the turbulence intensity of the ablation product gas injected into the boundary layer was finite and a function of the mass injection rate. The origin of turbulence of the injected gas could be attributed to rough surface, intermittent injection of the ablation product gas, and coalescence of injected jets through the char layer. He derived the functional form for the mixing length at the wall surface and determined the time constant by a comparison with the experimental data at the stagnation point where the boundary layer is otherwise laminar.

Izawa and Sawada implemented this injection-induced turbulence model in the existing computational fluid dynamics (CFD) code through a combination of two different eddy-viscosity models.[6] The near-wall behavior of the turbulent injection gas was described by the mixing length theory using the modified Van Driest damping function (see Ref. 7). The injection-induced turbulence model gives the boundary condition for this part of the combined eddy-viscosity model. The overall turbulent boundary layer except for the turbulent injection gas is described by the Baldwin–Lomax zero-equation model.[8] It was shown in the computation for a sphere with wall injection that the enhanced heat transfer rate at the stagnation point was well reproduced and that a higher heating rate in the downstream region was indicated.

This unique turbulence model was employed in the analyses of heating environment for the Pioneer-Venus probe vehicles. Because of the higher convective heating due to the enhanced turbulence effect, the temperature rise in the ablative heatshield at the frustum region was successfully reproduced.[9,10] This turbulence model, however, has not yet been attempted for the Galileo probe vehicle. In the Galileo case, the convective heating is far smaller than the radiative heating due to massive injection.[1,11] Therefore, the higher convective heating due to the enhanced turbulence effect that explained the temperature rise at the frustum region of the Pioneer-Venus probe vehicles does not seem applicable to the Galileo case directly. However, the promotion of turbulence in the shock layer and, hence, in the ablation layer due to the ablation product gas can alter various flow features considerably. It is interesting to examine the possible effects of injection-induced turbulence on the overall heat flux exerted on the Galileo probe vehicle.

In addition to the stated turbulence effect, there are several other issues that can alter the heating rate exerted on the Galileo probe vehicle while descending into the Jovian atmosphere. In the preflight prediction,[1] the helium mole fraction was assumed to be 11%, whereas the measured mole fraction was 13.6% (Refs. 12 and 13). This larger helium mole fraction can cause higher temperature in the shock layer in the actual flight. According to the study by Brewer and Brant,[14] this difference can increase the radiative heat flux by about 20% for the peak heating condition. Such higher radiative heating is expected to increase the amount of recession in the frustum region to yield a closer agreement to that of the flight data. However, this will cause further discrepancy in the stagnation region.

Yet another important physical process that has an impact on the surface heating rate is the nonequilibrium effect. Park and Tauber suggested the observed discrepancy in the recession profile at the stagnation region could be explained by the nonequilibrium effect.[4] Because a finite time elapses behind the shock wave before radiation emission occurs, the thickness of radiating gas is less than the actual shock-layer thickness.[15] As a result, radiative heat flux at the stagnation region can be reduced from that given by the preflight analysis, assuming thermochemical equilibrium to yield a closer agreement to that of the flight data. Note, however, that this nonequilibrium effect conversely reduces radiative heat flux over the frustum.

The ultimate purpose of the present study is to reproduce the surface recession data of the Galileo probe vehicle obtained during the entry flight into the Jovian atmosphere. We attempt to carry out a trajectory-based heating analysis of the entry flight accounting for both radiation and ablation. In the present study, however, we focus on the reproduction of the larger amount of recession observed at the frustum region in the flight data because we employ the thermochemical equilibrium assumption. The actual atmospheric composition is assumed in the present calculation to have a larger heating rate. Park's injection-induced turbulence model[5] is employed to see the consequence of how the enhanced turbulence effect due to the ablation product gas can increase radiative heat flux toward the wall at the frustum region. The obtained surface recession is compared with the flight data.

Numerical Method

Governing Equations

The governing equations are the Navier–Stokes equations in an axisymmetric form, which can be written as

$$\frac{\partial \boldsymbol{Q}}{\partial t} + \frac{\partial (\boldsymbol{F} - \boldsymbol{F}_v)}{\partial x} + \frac{\partial (\boldsymbol{G} - \boldsymbol{G}_v)}{\partial y} + (\boldsymbol{H} - \boldsymbol{H}_v) = \boldsymbol{H}_{\text{rad}} \tag{1}$$

The components of the conservative variables, the flux vectors, and the source vectors are given, respectively, as follows:

$$Q = \begin{bmatrix} \rho_f \\ \rho_a \\ \rho u \\ \rho v \\ E \end{bmatrix}, \qquad \boldsymbol{F} = \begin{bmatrix} \rho_f u \\ \rho_a u \\ \rho u^2 + p \\ \rho u v \\ (E + p)u \end{bmatrix}, \qquad \boldsymbol{G} = \begin{bmatrix} \rho_f v \\ \rho_a v \\ \rho u v \\ \rho v^2 + p \\ (E + p)v \end{bmatrix}$$

$$\boldsymbol{F}_v = \begin{bmatrix} -\rho_f u_f \\ -\rho_a u_a \\ \tau_{xx} \\ \tau_{xy} \\ \tau_{xx} u + \tau_{xy} v + \kappa \dfrac{\partial T}{\partial x} - \displaystyle\sum_{\text{species}} \rho_s u_s h_s \end{bmatrix}$$

$$\boldsymbol{G}_v = \begin{bmatrix} -\rho_f v_f \\ -\rho_a v_a \\ \tau_{xy} \\ \tau_{yy} \\ \tau_{xy} u + \tau_{yy} v + \kappa \dfrac{\partial T}{\partial y} - \displaystyle\sum_{\text{species}} \rho_s v_s h_s \end{bmatrix}$$

$$\boldsymbol{H} = \frac{1}{y} \begin{bmatrix} \rho_f v \\ \rho_a v \\ \rho u v \\ \rho v^2 \\ (E + p)v \end{bmatrix}$$

$$\boldsymbol{H}_v = \frac{1}{y} \begin{bmatrix} -\rho_f v_f \\ -\rho_a v_a \\ \tau_{xy} \\ \tau_{y\theta} \\ \tau_{xy} u + \tau_{yy} v + \kappa \dfrac{\partial T}{\partial y} - \displaystyle\sum_{\text{species}} \rho_s v_s h_s \end{bmatrix}$$

$$\boldsymbol{H}_{\text{rad}} = \begin{bmatrix} 0 \\ 0 \\ 0 \\ 0 \\ -\nabla q_{\text{rad}} \end{bmatrix} \tag{2}$$

In the study by Moss,[16] the viscous shock-layer equations consisting of the total mass, the elemental species mass, the momentum, and the total energy conservation equations for an equilibrium multicomponent gas mixture were considered. On the other hand, in this study, the mass conservation equations for the freestream gas (hydrogen–helium gas mixture) and that for the ablation product gas are solved, in which the ratio of the elemental concentration of each gas is assumed to be constant. Those subscripts f and a denote the freestream gas and the ablation product gas, respectively. We assume a binary diffusion between the freestream gas and the ablation product gas where the diffusion velocity of the present gas mixture is proportional to the gradient of the mass concentration C. Therefore, the x component of the diffusive flux for the freestream gas, for example, can be expressed as

$$\rho_f u_f = -\rho D_{fa} \frac{\partial C_f}{\partial x} \tag{3}$$

The binary diffusion coefficient D_{fa} is given by

$$D_{fa} = \mu / Sc\, \rho \tag{4}$$

where a constant Schmidt number Sc ($=0.582$) is assumed (see Ref. 1).

The governing equations are discretized by a finite volume method. The numerical flux function is given by the AUSM-DV scheme[17] with use of the MUSCL approach to attain a higher-order of spatial accuracy. A matrix-free lower–upper symmetric Gauss–Seidel method is employed for the implicit time integration, except for the radiative heat fluxes that are integrated explicitly (see Ref. 18).

Boundary Conditions

It is assumed that the ablation process is quasi steady. The mass injection rate is determined from an energy balance at the wall, which is given by

$$\dot{m} = (-q_{c,w} - q_{\text{rad,w}}) / \Delta H_a \tag{5}$$

The wall temperature is assumed to coincide with the sublimation temperature of the ablator. The sublimation temperature (in degrees Kelvin) and the heat of ablation for the carbon-phenolic ablator are calculated by the following expressions, respectively, as[1]

$$T_{\text{sub}} = 3797.0 + 342.0 \log p_w + 30.0 (\log p_w)^2 \tag{6}$$

$$\Delta H_a = 28.0 - 1.375 \log p_w + 27.2 (\log p_w)^2 \tag{7}$$

where p_w is the wall pressure in atmospheres. The composition of the carbon-phenolic ablator is assumed 92% carbon, 6% oxygen, and 2% hydrogen by mass.[1] The wall temperature and the mass injection rate are calculated iteratively while coupled with the flowfield calculation.

The surface recession rate is defined by

$$\Delta s = \dot{m} / \rho_v \tag{8}$$

where the density of virgin material is given by[3] $\rho_v = 1448$ kg/m^3. In the present calculation, the amount of the surface recession at each trajectory point is calculated by using a second-order formula based on the surface recession rates at the prior trajectory points. The computational meshes are generated at each trajectory point by considering the probe shape change.

For radiation calculation, the wall is treated as a gray surface with a reflectivity of 0.1 and an emissivity of 0.9. The far-field gas is assumed to be a blackbody at the freestream temperature.

Thermochemical Equilibrium Gas Properties

The equilibrium gas properties are calculated by the free-energy minimization technique.[19] The elemental species composition that is required for the free-energy minimization calculation is determined from the mass concentration of the freestream gas C_f and that of the ablation product gas C_a. Seven chemical species such as H_2, H, He, H_2^+, H^+, He^+, and e^- are considered to describe the freestream gas. An additional 18 species, C, C_2, C_3, C_4, C_5, C^+, CH, C_2H, C_3H, C_4H, C_5H, CH_2, C_2H_2, O, O_2, O^+, CO, and CO_2, are considered for the ablation product gas. The final chemical composition of these 25 chemical species is determined in the present calculation through the table lookup interpolation method.[20] The thermodynamic and transport properties of these chemical species are taken from Refs. 21–25.

Radiation Model

In the present multiband model, the absorption coefficients of the gas mixture are calculated at 4781 wavelength points for the wavelength range from 750 to 15,000 Å. These wavelength points are carefully selected to include all of the important atomic lines that participate in the energy transfer in the shock layer.[26] Continuum radiation, as well as absorption due to molecules, is also accounted for.

The absorption coefficient of the gas mixture is expressed as a sum of those for individual species, which is written as

$$k_\lambda = \sum_i n_i \sigma_\lambda^i \tag{9}$$

where n_i is the number density of species i and σ_λ^i is the absorption cross section per 1 mol/cm^3 of species i. The absorption cross section of individual species determined by the detailed line-by-line calculation[27] is first tabulated at the chosen wavelength points for the temperature range from 3000 to 17,000 K and for the electron number density range from 10^{10} to 10^{18} 1/cm^3. The temperature range is divided into 14 equal intervals, whereas the electron number density range is divided into 20 equal intervals in the logarithmic scale. In the actual flowfield computations, the absorption cross section at the local temperature and electron number density are determined from a bilinear interpolation of the tabulated data. This is in contrast to the conventional multiband radiation model for air in which the absorption cross section is determined from a curve fit depending only on the local temperature.[26] The present treatment is found necessary because the absorption cross section of atomic hydrogen depends critically on the electron number density because of the Stark broadening effect.

The validity of the present table lookup method for finding the absorption cross section in the multiband model is examined by comparing the calculated radiative heat flux profiles with those given by the detailed line-by-line calculations for various shock layer properties. Though not shown here, good agreements are obtained for the radiative heat flux profiles in the shock layer with varying temperature and electron number density. We also note that the multiband model for hydrogen–helium mixture constructed along the lines of the present method has been applied to solve the entry flight flowfield of the Galileo probe with radiation.[28] Ablation was not accounted for in that calculation. The obtained results showed reasonable agreement with that shown in the preflight prediction of Moss and Simmonds.[1]

In the present radiation calculation, the participating chemical species are H and H^+ for the freestream gas and, in addition, C, C_2, C_3, O, O_2, and CO for the ablation product gas. Radiation mechanisms included in the calculation are listed in Table 1.[27,29–34]

One-dimensional radiative transfer calculation using the tangent-slab approximation is employed in the present calculation to determine the radiative heat flux. A fully coupled calculation of the flowfield and radiation is carried out for obtaining a converged solution for the strongly radiating flowfield. To reduce the computing time, we employ the parallel computation for solving the radiative transfer equations[35] using a SGI ORIGIN 2000 with up to 128 processors.

Table 1 Radiation mechanisms involved in the present radiation model

Species	System	Source
	Atomic lines	
H	Lyman, Balmer, and Paschen series	29,30
C	710 lines	27,30
O	564 lines	27,30
	Molecular bands	
C_2	Swan, Ballik-Ramsay, Fox-Herzberg, Freymark, Mulliken, Deslandres-d'Azambuja, Phillips	27
CO	4^+, Hopfield-Brige	27
O_2	Schumann-Runge	31
C_3	Swings, UV	27,32
	Bound-free continuum	
H		33,34
C	600–62,000 Å	27,31
O	500–10,000 Å	31
	Free–free continuum	
H, H^+		30,34

Turbulence Model

The injection-induced turbulence model is implemented into the present CFD code to yield the overall eddy viscosity as[9,10]

$$\mu_t = (\mu_t)_{\mathrm{BL}} + (\mu_t)_{\mathrm{inj}} \tag{10}$$

where the first term is given by the original form of the Baldwin–Lomax turbulence model.[8] The second term is given by

$$(\mu_t)_{\mathrm{inj}} = \rho d_{\mathrm{inj}}^2 |\omega| \tag{11}$$

$$d_{\mathrm{inj}} = \max(0, d_w - \chi y) \exp(-y^+/A^+) \tag{12}$$

The mixing length d_{inj} takes the maximum value d_w at the wall and decays exponentially in the boundary layer according to the Van Driest theory. The wall mixing length d_w is chosen to satisfy the following relation:

$$(\mu_{t,w})_{\mathrm{Park}} = \rho_w d_w^2 |\omega|_w \tag{13}$$

where $(\mu_{t,w})_{\mathrm{Park}}$ is the eddy viscosity at the wall with injection flow. Park determined this as[5]

$$(\mu_{t,w})_{\mathrm{Park}} = 0.4 \dot{m} d \tag{14}$$

where the mixing length d is simply given by

$$d = \tau \dot{m}/\rho_w \tag{15}$$

The time constant τ is taken to be 2×10^{-4} s. Details of the injection-induced turbulence model are described in Ref. 5. The turbulent Prandtl number and Lewis number are assumed to be 0.9 and 1.0, respectively.[1]

Flow Conditions

Calculations are carried out at eight trajectory points chosen along the actual entry trajectory.[2] The freestream conditions for each trajectory point are listed in Table 2. The freestream composition is assumed to be 86.4% H_2 and 13.6% He by volume. Figure 4 shows a typical example of the computational meshes with 51×71 grid points. At the shock position, grid lines are clustered to resolve the detached shock wave sharply. In the present calculations, a Courant–Friedrichs–Lewy number of 1000 is assumed.

Results and Discussion

In Fig. 5, the final recession data obtained in the present calculation is compared with the flight data[2] and that obtained in the study by Moss and Simmonds.[1] At the stagnation point, the calculated final recession overestimates the flight data considerably, although it agrees with that given by Moss and Simmonds.[1] At the frustum region, on the other hand, the obtained final recession closely reproduces the flight data.

Table 2 Flow conditions at the trajectory points[2]

Time, s	Altitude, km	Velocity, km/s	Density, kg/m^3
40.35	190	46.951	3.16×10^{-5}
43.79	170	46.256	7.03×10^{-5}
47.36	150	44.813	1.49×10^{-4}
49.21	140	43.531	2.27×10^{-4}
51.16	130	41.591	3.49×10^{-4}
53.23	120	38.617	5.56×10^{-4}
55.52	110	34.296	8.36×10^{-4}
58.19	100	28.440	1.23×10^{-3}

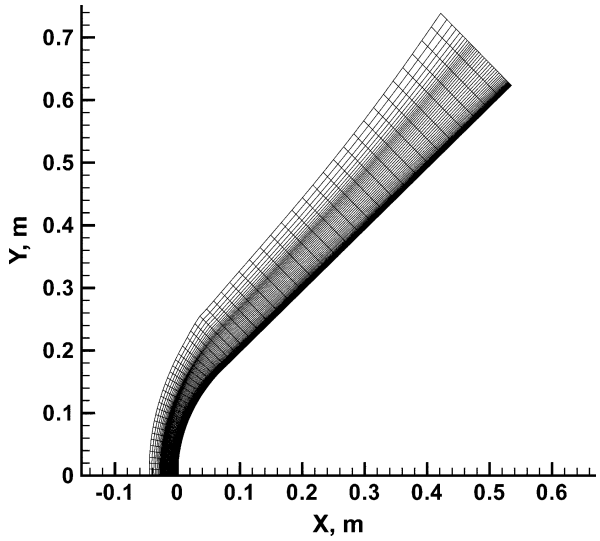

Fig. 4 Computational 51 × 71 grid point mesh used in calculation at 51.16 s.

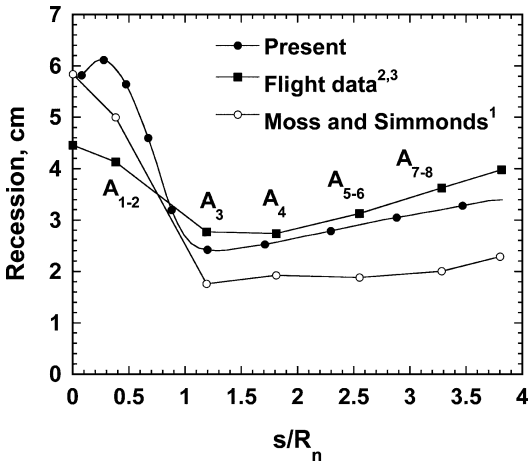

Fig. 5 Comparison of obtained final forebody recession profile with flight data and preflight prediction.

Figures 6a–6c show various flowfield properties at the peak heating point (51.16 s) along the line normal to the wall at the ARAD sensors locations, as well as at the stagnation point. Figure 6a shows the temperature profiles. The shock-layer temperature reaches 16,000 K at the stagnation region, whereas it is 13,000 K at the frustum region. However, note that the gas temperature in the near-wall region is lower at the stagnation point than that at the other sensor locations. Figure 6b shows the mass fraction of the ablation product gas. Toward the frustum region, the ablation product gas penetrates deeper into the shock layer due to diffusion. At the stagnation point, the mass fraction of the ablation product gas is rather abundant in the near-wall region, whereas it sharply decreases as departing from the wall surface in the downstream region. Figure 6c shows the wallward radiative heat flux profiles. At the stagnation point, significant absorption of the radiative heat flux occurs in the near-wall region. The attenuation due to absorption is as large as 55% with respect to the peak value. At the frustum region, on the other hand, the attenuation amounts only to about 25% because of the weaker absorption.

Figures 7a and 7b show the spectral intensity reaching the wall surface at the stagnation point and at the location of ARAD 7-8, respectively. The spectral intensity is obtained by the line-by-line transport calculation[27] using the converged flowfield solution. At the stagnation point, one sees that C_3 UV bands significantly absorb radiation in the wavelength range from 1400 to 2000 Å. Absorption due to C_3 Swings band is also observed from 3000 to 5000 Å. The

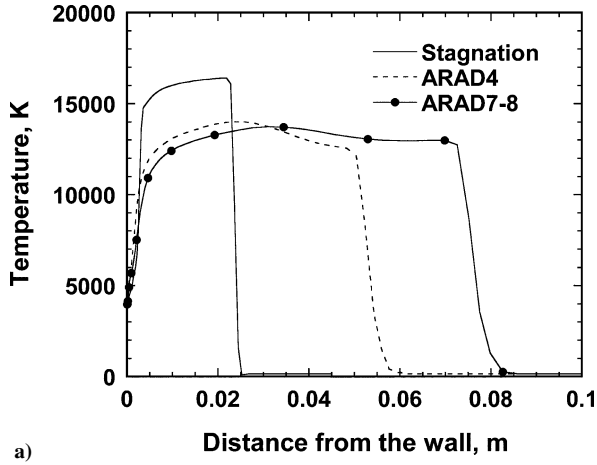

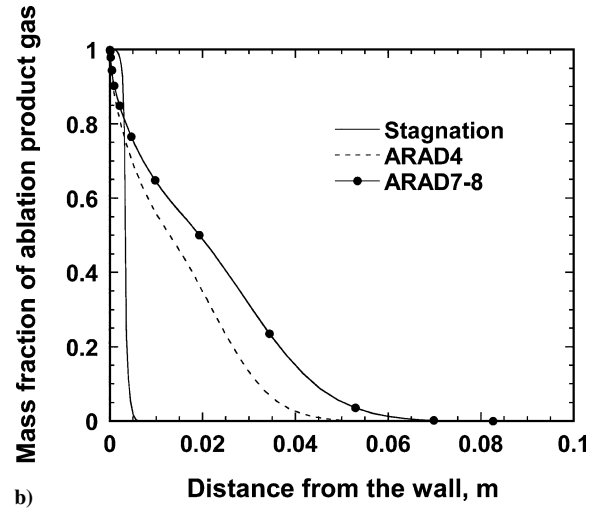

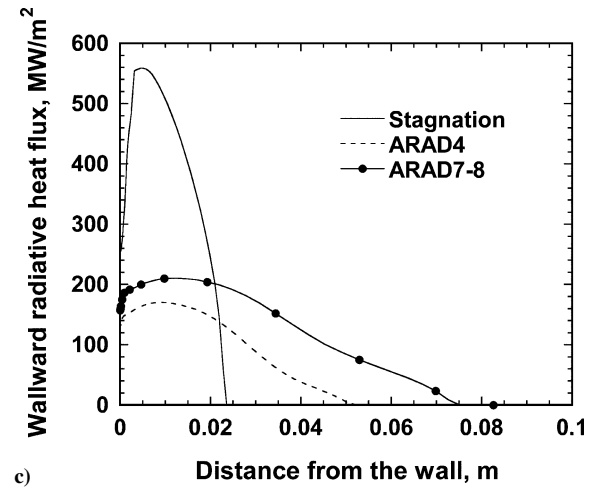

Fig. 6 Flowfield properties along the line normal to the wall at the peak heating point, 51.16 s: a) temperature distributions, b) mass fraction distributions of ablation product gas, and c) wallward radiative heat flux distributions.

H_β line of atomic hydrogen at 4800 Å is partially absorbed by the C_2 Swan band system. At the frustum region, on the other hand, absorption due to C_2 and C_3 band systems are not as significant compared with that at the stagnation region. Note that many atomic carbon lines in the wavelength range from 1400 to 2000 Å and above 7000 Å reach the wall at the frustum region. These emissions come from the high-temperature shock-layer region where the ablation product gas is reached due to diffusion effect as shown in Fig. 6b.

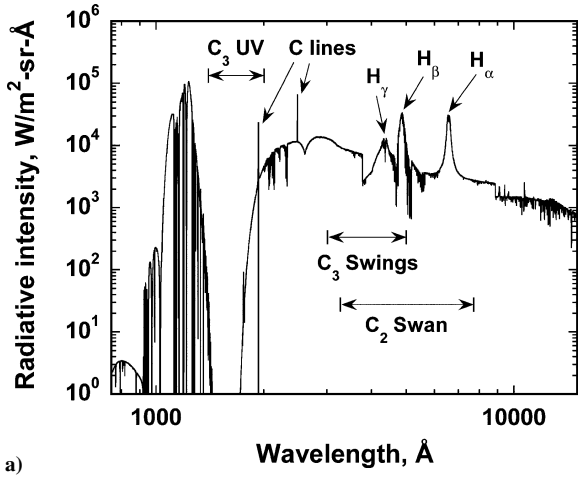

a)

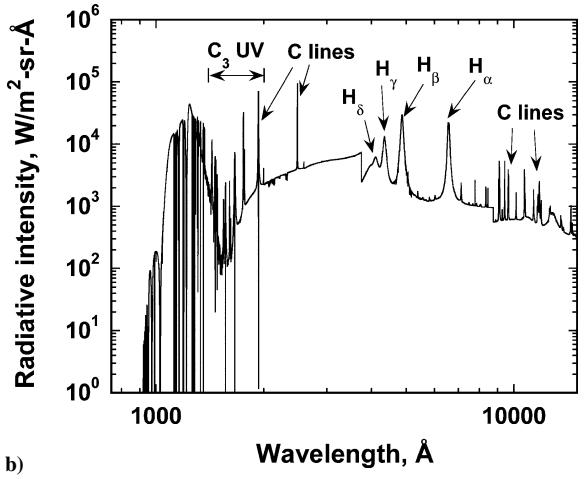

b)

Fig. 7 Spectral intensity reaching the wall at peak heating point, 51.16 s: a) stagnation point and b) ARAD7-8.

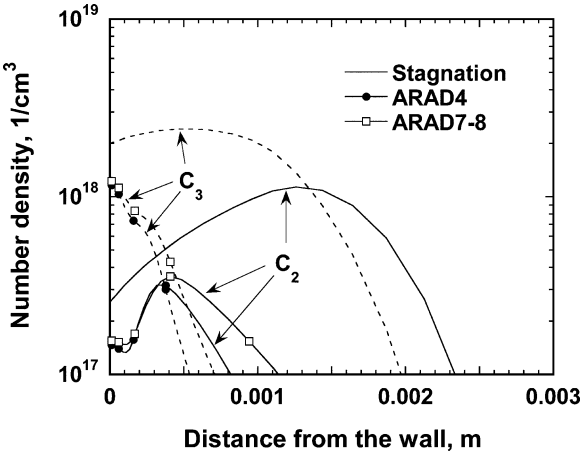

Fig. 8 Number density distributions of C_2 and C_3 along line normal to wall at peak heating point, 51.16 s.

The number density distributions of C_2 and C_3 in the near-wall region along the line normal to the wall at the locations of ARAD sensors as well as at the stagnation point are indicated in Fig. 8. Because the temperature in the near-wall region becomes higher at the frustum region as indicated in Fig. 6a, those C_2 and C_3 are likely dissociated and can only remain in the vicinity of the wall. This reduces the absorption of radiation considerably at the frustum region.

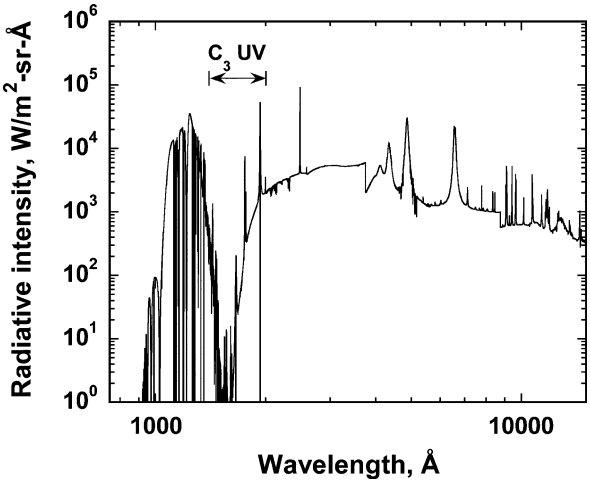

Fig. 9 Spectral intensity reaching the wall at the location of ARAD7-8 (injection-induced turbulence model not included).

Now it becomes clear that the large recession in the frustum region in the present calculation is due to a large radiative heat flux caused by the weak absorption there, which is due to the reduced number densities of C_2 and C_3 in the near-wall region. The reduction of C_2 and C_3 can occur either by dissociation due to the high temperature in the near-wall region or by the diffusion of the ablation product gas. We have seen in Fig. 6a that higher temperature that promotes dissociation appears in the near-wall region. We also have seen in Fig. 6b that the mass fraction of the ablation product gas rapidly decreases due to the diffusion in the near-wall region, except at the stagnation point. Therefore, it is necessary to identify the reason why these effects that contribute to reduce the number densities of C_2 and C_3 occur rather significantly in the present calculation.

Figure 9 shows the spectral intensity reaching the wall surface at the location of ARAD 7-8 obtained from the converged flowfield solution that does not take account of the injection-induced turbulence model. The helium mole fraction is assumed to be 13.6%. Comparison with the result shown in Fig. 7b in which the effect of injection-induced turbulence is accounted for reveals that strong absorption by C_3 UV bands occurs in the wavelength region from 1400 to 2000 Å. The comparison of the mass fraction profiles of the ablation product gas in the near-wall region at the location of ARAD 7-8 is shown in Fig. 10a. When the injection-induced turbulence model is included in the calculation, the fraction of the ablation product gas is reduced significantly in the near-wall region due to an enhanced diffusion effect. This can be confirmed in Fig. 10b, in which the normalized eddy-viscosity distributions in the near-wall region at ARAD 4 as well as at ARAD 7-8 are shown. Note that the eddy viscosity in the near-wall region is significantly increased when the injection-induced turbulence model is combined with the Baldwin–Lomax turbulence model. Figure 10c shows the number density distributions of C_2 and C_3 in the near-wall region at the location of ARAD 7-8. When the injection-induced turbulence model is included in the calculation, the number densities of C_2 and C_3 are significantly decreased in the near-wall region. All of these results indicate that the larger eddy viscosity in the near-wall region caused by the injection-induced turbulence model enhances the diffusion effect that reduces the mass fraction of the ablation product gas in the near-wall region, increases the temperature to promote dissociation reactions of C_2 and C_3, and makes the absorption of radiation weaker.

In Ref. 4, Park and Tauber pointed out several possible reasons for observed difference in the final recession profile between that deduced from the flight data of the Galileo probe and that of the preflight prediction at the frustum region. Though we do not deny other possible reasons, we emphasize here that the enhanced turbulence effect due to the ablation product gas can give a consistent explanation of why the radiative heat flux is increased at the frustum region. We also emphasize that a reasonable agreement is obtained

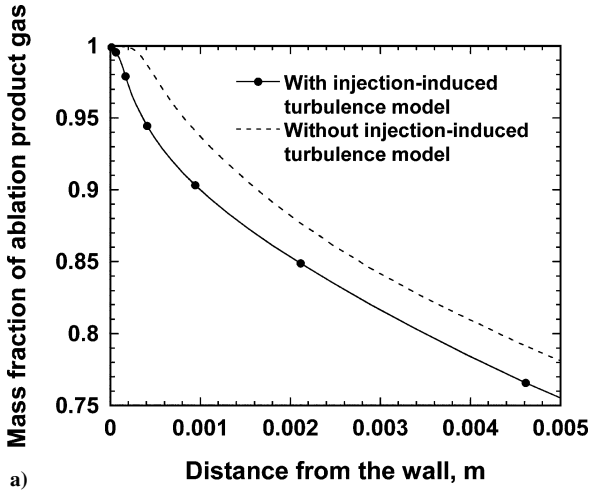

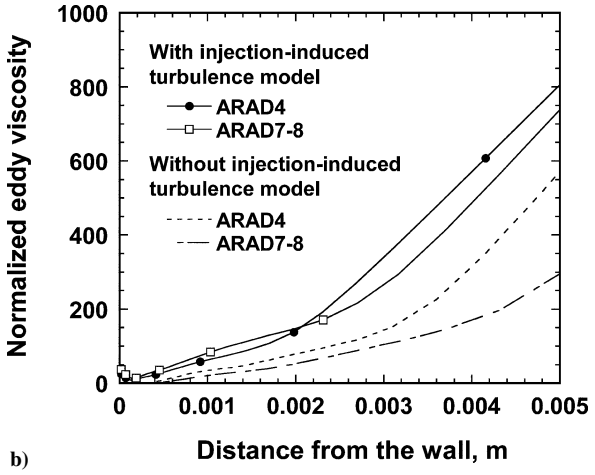

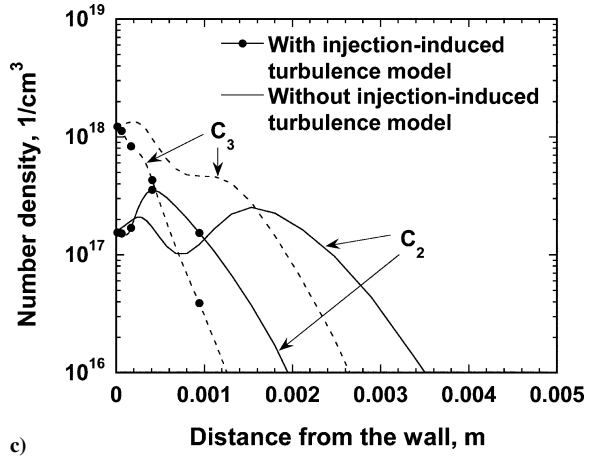

Fig. 10 Effect of injection-induced turbulence model on flowfield properties in near-wall region at ARAD7-8: a) mass fraction distributions of ablation product gas, b) normalized eddy viscosity distributions, and c) number density distributions of C_2 and C_3.

for the first time between the calculated final recession profile at the frustum region and that of the flight data when we employ the injection-induced turbulence model.

Let us compare the overall influences of changing the atmospheric composition and also of introducing the injection-induced turbulence model on the surface radiative heat flux at the peak heating point (51.16 s). In Fig. 11, four cases are compared for the forebody radiative heat flux. The present calculation, in which the helium

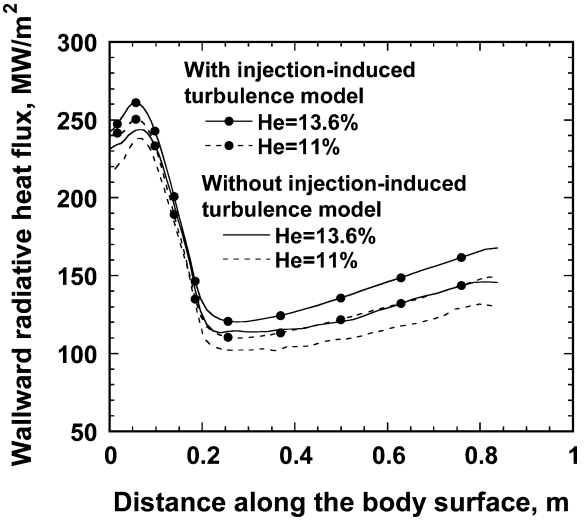

Fig. 11 Influences of changing atmospheric composition and introducing injection-induced turbulence model on forebody radiative heat flux distributions.

mole fraction is assumed to be 13.6% and the injection-induced turbulence model is employed, gives the highest radiative heat flux among these four cases. On the other hand, if the helium mole fraction is assumed to be 11.0% and the injection-induced turbulence model is not used, we have the lowest radiative heat flux. This case corresponds to that given by Moss and Simmonds.[1] The case with the helium fraction of 13.6% but the injection-induced turbulence model not used gives the averaged value of the earlier two cases. This almost agrees with the result given by Brewer and Brant.[14] The remaining case of assuming the helium fraction to be 11.0% with the injection-induced turbulence model considered in the calculation gives the radiative heat flux distribution that almost duplicates the preceding result. From these results, therefore, both the increased helium fraction in the freestream gas and also the consideration of the injection-induced turbulence model in the calculation are equally contributing to increase the radiative heat flux at the frustum region.

Finally, the following remarks are noted. First, it is found that the convective heat fluxes at ARAD sensor locations are almost diminished at all trajectory points due to massive ablation, even if we consider the effect of injection-induced turbulence in the calculations. Therefore, the net heat flux virtually agrees with that of the radiative heat flux. Second, besides the nonequilibrium effect mentioned earlier, the radiative heat flux at the stagnation region can be reduced if we determine the radiative heat flux accounting for the multidimensional radiative transfer.[28] The tangent-slab approximation used in the present calculation is known to yield a larger amount of radiative heat flux at the stagnation region for a typical radiating flowfield over a blunt body. Last, we note that the amount of the final recession obtained in the present calculation still underestimates the flight data slightly at the frustum region. The radiative heat flux at the frustum region can be increased if we consider the spalled particles from the ablator surface because those spalled particles not only enhance the turbulence intensity in the shock layer, but also to emit radiation while heated in the shock layer.[36,37] The significance of these effects due to spalled particles, however, needs to be clarified.

Conclusions

A trajectory-based heating analysis of the Galileo probe entry flowfield with radiation and ablation is successfully carried out. The flowfield is assumed to be in thermochemical equilibrium. The radiative energy transfer calculation is tightly coupled with the flowfield calculation, where the absorption coefficients of the gas mixture are given by the multiband radiation model. The injection-induced turbulence model is employed to account for the enhanced turbulence effect due to the ablation product gas. It is shown in the present calculation that the final recession profile of the flight data at the

frustum region can be closely reproduced if we employ the injection-induced turbulence model, although that at the stagnation region is overestimated. It is indicated that the larger eddy viscosity caused by the injection-induced turbulence model enhances the diffusion effect that reduces the mass fraction of the ablation product gas in the near wall region, increases the temperature to promote dissociation reactions of C_2 and C_3, and makes the absorption of radiation weaker.

Acknowledgments

All of the calculations in the present study are carried out using the ORIGIN 2000 at the Institute of Fluid Science, Tohoku University.

References

[1]Moss, J. N., and Simmonds, A. L., "Galileo Probe Forebody Flowfield Prediction," *Entry Vehicle Heating and Thermal Protection Systems: Space Shuttle, Solar Starprobe, Jupiter Galileo Probe*, edited by P. E. Bauer and H. E. Collicott, Vol. 85, Progress in Astronautics and Aeronautics, AIAA, New York, 1983, pp. 419–445; also AIAA Paper 82-0874, June 1982.

[2]Milos, F. S., "Galileo Probe Heat Shield Ablation Experiment," *Journal of Spacecraft and Rockets*, Vol. 34, No. 6, 1997, pp. 705–713.

[3]Milos, F. S., Chen, Y.-K., Squire, T. H., and Brewer, R. A., "Analysis of Galileo Probe Heatshield Ablation and Temperature Data," *Journal of Spacecraft and Rockets*, Vol. 36, No. 3, 1999, pp. 298–306.

[4]Park, C., and Tauber, M. E., "Heatshielding Problems of Planetary Entry, A Review," AIAA Paper 99-3415, July 1999.

[5]Park, C., "Injection-Induced Turbulence in Stagnation Point Boundary Layers," *AIAA Journal*, Vol. 22, No. 2, 1984, pp. 219–225.

[6]Izawa, Y., and Sawada, K., "Calculation of Surface Heat Transfer for a Sphere with Wall Injection," *Journal of Thermophysics and Heat Transfer*, Vol. 14, No. 2, 2000, pp. 230–236.

[7]Cebeci, T., "Behavior of Turbulent Flow near a Porous Wall with Pressure Gradient," *AIAA Journal*, Vol. 8, No. 12, 1970, pp. 2152–2156.

[8]Baldwin, B. S., and Lomax, H., "Thin Layer Approximation and Algebraic Model for Separated Turbulent Flows," AIAA Paper 78–257, Jan. 1978.

[9]Izawa, Y., and Sawada, K., "Calculation of Hypersonic Flow with Ablation for Pioneer-Venus Probe," AIAA Paper 2000-0208, Jan. 2000.

[10]Takahashi, M., and Sawada, K., "Simulation of Entry Flight Flowfield over Four Probe Vehicles in Pioneer-Venus Mission," AIAA Paper 2002-0909, Jan. 2002.

[11]Moss, J. N., Hones, J. J., and Simmonds, A. L., "Radiative Flux Penetration Through a Blown Shock Layer for Jupiter Entry," *Outer Planet Entry Heating and Thermal Protection*, edited by R. Viskanta, Vol. 64, Progress in Astronautics and Aeronautics, AIAA, New York, 1979, pp. 22–41; also AIAA Paper 78-908, May 1978.

[12]Von Zahn, U., and Hunten, D. M., "The Helium Mass Fraction in Jupiter's Atmosphere," *Science*, Vol. 272, No. 5263, May 1996, pp. 849–851.

[13]Niemann, H. B., Atreya, S. K., Carignan, G. R., Donahue, T. M., Haberman, J. A., Harpold, D. N., Hartle, R. E., Hunten, D. M., Kasprzak, W. T., Mahaffy, P. R., Owen, T. C., Spencer, N. W., and Way, S. H., "The Galileo Probe Mass Spectrometer: Composition of Jupiter's Atmosphere," *Science*, Vol. 272, No. 5263, May 1996, pp. 846–849.

[14]Brewer, R. A., and Brant, D. N., "Thermal Protection System for the Galileo Mission Atmospheric Entry Probe," *Thermophysics of Atmospheric Entry*, edited by A. L. Crosbie, Vol. 77, Progress in Astronautics and Aeronautics, AIAA, New York, 1981, pp. 309–334; also AIAA Paper 80-0358, 1980.

[15]Leibowitz, L. P., "Measurements of the Structure of an Ionizing Shock Wave in a Hydrogen–Helium Mixture," *Physics of Fluids*, Vol. 16, No. 1, 1973, pp. 59–68.

[16]Moss, J. N., "Radiative Viscous-Shock-Layer Solutions with Coupled Ablation Injection," *AIAA Journal*, Vol. 14, No. 9, 1976, pp. 1311–1317.

[17]Wada, Y., and Liou, M. S., "A Flux Splitting Scheme with High-Resolution and Robustness for Discontinuities," NASA TM-106452, Jan. 1994; also AIAA Paper 94-0083, Jan. 1994.

[18]Tsuru, T., and Sawada, K., "Convergence Issues on Fully-Coupled Radiative Gas Dynamic Calculations," AIAA Paper 2000-0732, Jan. 2000.

[19]Gordon, S., and McBride, B. J., "Computer Program for Calculation of Complex Chemical Equilibrium Compositions and Applications," NASA RP-1311, Oct. 1994.

[20]Liu, Y., and Vinokur, M., "Equilibrium Gas Flow Compositions. I. Accurate and Efficient Calculation of Equilibrium Gas Properties," AIAA Paper 89-1736, June 1989.

[21]McBride, B. J., Zehe, M. J., and Gordon, S., "NASA Glenn Coefficients for Calculating Thermodynamic Properties of Individual Species," NASA TP-2002-211556, Sept. 2002.

[22]Duff, R. E., and Bauer, S. H., "Equilibrium Composition of C/H System at Elevated Temperatures," *Journal of Chemical Physics*, Vol. 36, No. 7, 1962, pp. 1754–1767.

[23]Svehla, R. A., "Transport Coefficients for the NASA Lewis Chemical Equilibrium Program," NASA TM-4647, April 1995.

[24]Zoby, E. V., Graves, R. A., Jr., Moss, J. N., Kumer, A., and Simmonds, A., "Transport Property Correlations for H_2–He Gas Mixtures at Temperatures of 1000–25,000 K," *AIAA Journal*, Vol. 18, No. 4, 1980, pp. 463–470.

[25]Gupta, R. N., Lee, K.-P., Moss, J. N., and Sutton, K., "Viscous Shock-Layer Solutions with Coupled Radiation and Ablation for Earth Entry," *Journal of Spacecraft and Rockets*, Vol. 29, No. 2, 1992, pp. 173–181; also AIAA Paper 90-1697, June 1990.

[26]Park, C., and Milos, F. S., "Computational Equations for Radiating and Ablating Shock Layers," AIAA Paper 90-0356, Jan. 1990.

[27]Arnold, J. O., Cooper, D. M., Park, C., and Prakash, S. G., "Line-by-Line Transport Calculations for Jupiter Entry Probes," *Entry Heating and Thermal Protection*, edited by W. B. Olstad, Vol. 69, Progress in Astronautics and Aeronautics, AIAA, New York, 1980, pp. 52–82; also AIAA Paper 79-1082, 1979.

[28]Matsuyama, S., Shimogonya, Y., Ohnishi, N., Sawada, K., and Sasoh, A., "Numerical Simulation of Galileo Probe Entry Flowfield with Radiation," AIAA Paper 2002-2994, June 2002.

[29]Stehle, C., and Hutcheon, R., "Extensive Tabulation of Stark Broadened Hydrogen Line Profiles," *Astronomy and Astrophysics Supplement Series*, Vol. 140, No. 1, Nov. 1999, pp. 93–97.

[30]Fujita, K., and Abe, T., "SPRADIAN, Structured Package for Radiation Analysis: Theory and Application," Inst. of Space and Astronautical Science, Rept. 669, Kanagowa, Japan, Sept. 1997.

[31]Park, C., "Nonequilibrium Air Radiation (NEQAIR) Program: User's Manual," NASA TM-86707, July 1985.

[32]Shinn, J. L., "Optical Absorption of Carbon and Hydrocarbon Species from Shock Heated Acetylene and Methane in the 135–220 nm Wavelength Range," *Thermophysics of Atmospheric Entry*, edited by T. E. Horton, Vol. 82, Progress in Astronautics and Aeronautics, AIAA, New York, 1982, pp. 68–80; also AIAA Paper 81-1189, 1981.

[33]Zeldovich, Y. B., and Raizer, Y. P., *Physics of Shock Waves and High-Temperature Hydrodynamic Phenomena*, Dover, New York, 1990, pp. 269–272.

[34]Menzel, D. H., and Pekeris, C. L., "Absorption Coefficients and Hydrogen Line Intensities," *Monthly Notices of the Royal Astronomical Society*, Vol. 96, Nov. 1935, pp. 77–111.

[35]Matsuyama, S., Sakai, T., Sasoh, A., and Sawada, K., "Parallel Computation of Fully Coupled Hypersonic Radiating Flowfield Using Multiband Model," *Journal of Thermophysics and Heat Transfer*, Vol. 17, No. 1, 2003, pp. 21–28.

[36]Davies, C. B., and Park, C., "Trajectories of Solid Particles Spalled from a Carbonaceous Heat Shield," *Entry Vehicle Heating and Thermal Protection Systems: Space Shuttle, Solar Starprobe, Jupiter Galileo Probe*, edited by P. E. Bauer and H. E. Collicott, Vol. 85, Progress in Astronautics and Aeronautics, AIAA, New York, 1983, pp. 472–495.

[37]Park, C., "Interaction of Spalled Particles with Shock Layer Flow," *Journal of Thermophysics and Heat Transfer*, Vol. 13, No. 4, 1999, pp. 441–449.